



# Fabricable concentric-ring metalens with high focusing efficiency based on two-dimensional subwavelength unit splicing

CHENGMIAO WANG,<sup>1</sup>  YU LIN,<sup>1</sup>  YEMING HAN,<sup>1</sup> YUPEI WEI,<sup>1,2</sup>  
BIN WANG,<sup>1</sup> ZHAO JIN,<sup>3</sup> AND YONGBO DENG<sup>1,\*</sup>

<sup>1</sup>Changchun Institute of Optics, Fine Mechanics and Physics, Chinese Academy of Sciences, Changchun 130033, China

<sup>2</sup>University of Chinese Academy of Sciences, Beijing 100049, China

<sup>3</sup>School of Opto-electric Engineering, Changchun University of Science and Technology, Changchun 130022, China

\*dengyb@ciomp.ac.cn

**Abstract:** To address the challenges posed by computational resource consumption and data volume in the development of large-aperture metalenses, a design method for concentric-ring metalens based on two-dimensional unit splicing is proposed in this paper. In the method, the unit structure library is constructed through global traversal under the machining process constraints. The phase matching is performed for two polarization states with specific weights and the design of binary-height, concentric-ring structures with arbitrary polarization sensitivity is realized, whose focusing efficiency (the encircled power within  $3\times\text{FWHM}$  of the focal spot divided by the near-field outgoing power) is up to 90%. Based on this method, a polarization-insensitive metalens with a design wavelength of  $10\mu\text{m}$ , diameter of 2 cm, and numerical aperture of 0.447 is obtained. The method combines the advantages of lower computation requirements for a building block array of a metalens and lower structure data for a concentric-ring metalens. Consequently, it becomes possible to reduce calculation and processing costs by several orders of magnitude during the development process of metalenses with diameters ranging from  $10^3$  to  $10^5$  wavelengths. The resulting focusing efficiency can approach the upper limit achievable through global structural optimization and significantly surpass that of binary-height Fresnel lenses.

© 2023 Optica Publishing Group under the terms of the [Optica Open Access Publishing Agreement](#)

## 1. Introduction

Modern optical imaging systems are increasingly prioritizing lightweight and integrated designs, imposing stringent restrictions on the size and weight of optical components. Unlike traditional optical components, metalenses offer a unique approach by manipulating the energy and phase profile of light through subwavelength nanostructures [1,2]. They have many advantages in terms of low cost, easy integration and high imaging resolution, making them well-suited for emerging applications requiring micro-imaging system such as intelligent driving, wearable devices and robotics, which effectively address the growing need for lightweight solutions in diverse fields [3–5].

Building block array is the most common structure adopted for metalenses, wherein each unit comprises one or more dielectric nano-posts that resemble truncated waveguides aligned along the direction of light propagation. The dielectric posts concentrate the light field energy more effectively than the air gaps between them, allowing for the disregard of electromagnetic coupling between adjacent units [6,7]. This fundamental principle shifts the design focus from optimizing the overall metalens structure to the local design of individual units. Benefiting from the diversity of the shapes of nano-posts within each unit, the array-type metalenses exhibit undeniable advantages in broadband achromatic [8–12], high efficiency focusing with large NA

[13–15] and polarization correlation imaging [16–18]. A fly in the ointment is that the array-type metalenses with diameters up to thousands of wavelengths have up to  $10^7 \sim 10^9$  nano-posts, and their cross-section shapes become complicated while the ultimate optical properties are pursued. For the above reasons, the design layouts usually involve vast amount of data (ranging from hundreds of gigabytes to several terabytes), posing substantial challenges in terms of processing time and costs.

The concentric-ring metalens is composed of a series of concentric-ring structures with widths on the scale of wavelengths or subwavelengths [19,20]. Since the subwavelength-scale structure exists only in radial dimension but not in angular dimension, it can be regarded as the combination of array-type metalens composed of subwavelength structures and concentric-ring diffractive lens without subwavelength structures. The design and simulation process of the central-symmetric structure only needs to be carried out in the 2D cross-section containing lens diameter. Through the meticulous adjustment of the cross-section structure, the concentric-ring metalens can achieve diffraction limit imaging for monochromatic or polychromatic light. However, the structure of concentric-ring metalens is generally calculated as a whole using various reverse design algorithm [21–23], resulting in high computational resource requirements for the concentric-ring metalens with aperture above thousand wavelengths, and consuming weeks or even months of time costs.

In order to simultaneously solve the problem of extensive computational requirements of concentric-ring metalens and voluminous data associated with array-type metalens, this paper proposes an efficient and fast method to obtain the metalens structure. The core of this method lies in design the subwavelength scale “two-dimensional meta-atoms” within the profile of the concentric-ring metalens. In the design procedure, the subwavelength 2D units are firstly screened according to the restrictions of machining process, and a solving model of Helmholtz equation was established to characterize the complex amplitude response of the fabricable units to the background field with different polarization states. Then the phase matching with arbitrary weights is carried out for the dual polarization states to splice the metalens profile by a large number of 2D units. By rotating the profile around the axis of symmetry, the overall 3D structure of the concentric-ring metalens can be finally obtained.

## 2. Design method

The structural optimization of 3D building blocks is typically the key point of the array-type metalens design, in which the desired complex transmittances can be achieved by adjusting the size parameters of the nano-posts. However, the design structure may not be the optimal solution given the constraints of basic geometric shapes and topology limitations imposed by specific manufacturing processes. In contrast, the structural design of 2D units is essentially to solve 1D binary sequences, resulting in a significantly smaller computational scale compared to that of 3D building blocks, which makes it possible to optimize the unit structures based on the global traversal. In the design section, machinable unit structures are firstly screened and optical property calculation is completed subsequently. The simulation model is shown in Fig. 1.

In the unit structure simulation model, the working wavelength is set as  $\lambda=10\mu\text{m}$ , the typical wavelength of Long Wave Infrared (LWIR). The structural height of concentric rings is set as  $H=4.13\mu\text{m}$  to ensure the phase modulation amount of at least  $2\pi$  over a multi-wavelength scale. The refractive index of the monocrystalline silicon used is 3.42. The size of the structured grid is set to  $L_m=345\text{ nm}$  and the overall width of the simulation model is set as  $L=14L_m$ , which is less than  $0.5\lambda$  to ensure that phase matching at the edge of metalenses with large NA satisfies the Nyquist sampling theorem. The width of the design domain, denoted as  $L_d$ , is equal to  $L-2L_m$ . In the design domain, the material distribution can be defined on a 1D design line with a length of  $L_d$  and  $L_d/L_m$  discrete grids, where “1” and “0” are specified to represent whether the material or air is present at each grid, respectively. Consequently, all unit structures can be represented by 12-bit binary strings.

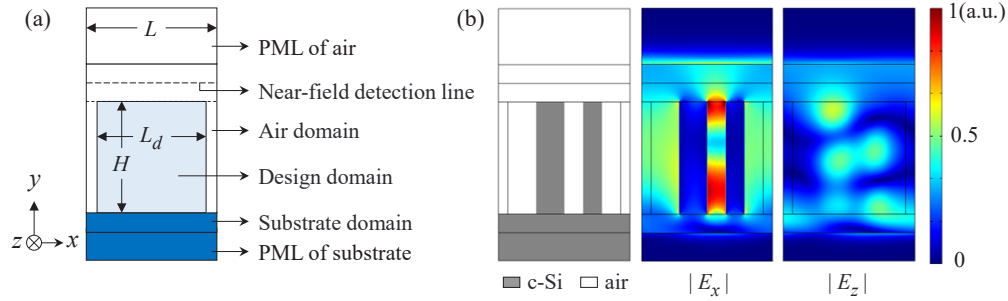


**Fig. 1.** (a) Geometric diagram of two dimensional unit simulation model; (b) The normalized  $|\mathbf{E}|$  field in  $x$  (TE state) and  $z$  (TM state) directions drawn with the structure “000111001100” as an example.

The machinability of unit structures can be determined using the exhaustive method: The minimum feature size limited by the processing technology is assumed to be  $N \cdot L_m$ . If there is a substring of the same character with a continuation length less than  $N$  bits in the structural string, the corresponding unit is considered non-processable and is excluded. Taking into account the machining limit of the step lithography process,  $N=2$  is taken in our work. As a result, all units containing substrings “101”, “010”, or beginning with “10”, ending with “01” are considered to contain the structures that are too small to be processed and need to be screened out, while the remaining machinable structures are retained for optical property characterization.

In this paper, COMSOL Multiphysics 6.0 software was used to construct the scattering field simulation model based on the finite element method. The upper and lower edges of the model are perfectly matched layers (PML) of substrate and air, respectively, which are used to truncate the simulation domain and eliminate the false boundary reflections. Both sides of the model are set to continuity boundary conditions. The background field contains TE and TM waves of equal intensity and the total scattering field of the processable unit structures are solved according to the Helmholtz equation. The complex transmittance is calculated at the position of the near-field exit pupil plane, then a unit structure library containing complete optical information is constructed accordingly. Their amplitude transmittances and modulated phases are shown in Fig. 2. In this work, the total number of all unit structures is about 4000, but the number of machinable structures is only about 100. The overall time required for structure screening and optical property simulation was only a few minutes, which proves the tremendous advantage of the exhaustive method in saving computing resources.

2D units have different phase modulation characteristics for TE and TM polarization, which is one of the main differences from 3D building blocks, thus it is theoretically impossible to make the phase of two polarization states simultaneously meet the hyperbolic phase required for ideal focusing. Furthermore, the modulation phase of TE state is less sensitive to structural changes, and cannot cover all values from  $-\pi$  to  $\pi$  under the limitation of processing technology and mechanical structure stability, as shown in Fig. 2(b). In order to reduce the loss of focusing efficiency caused by the above problem, the focusing weights  $W_{TE}$  and  $W_{TM}$  are set respectively in the process of unit splicing, and there are  $W_{TE} > 0$ ,  $W_{TM} > 0$ , and  $W_{TE} + W_{TM} = 1$ , representing the tendentiousness to give priority to improving the focusing efficiency. When  $W_{TE}$  and  $W_{TM}$  are 1, 0 or 0, 1 respectively, that is, single polarization state focusing, the ideal normalized complex amplitude of TM (TE) state is shown in Eq. (1):

$$\tilde{E}_0(x) = \exp \left[ -\frac{2\pi i}{\lambda} \sqrt{x^2 + F^2} + \Psi \right] \quad (1)$$

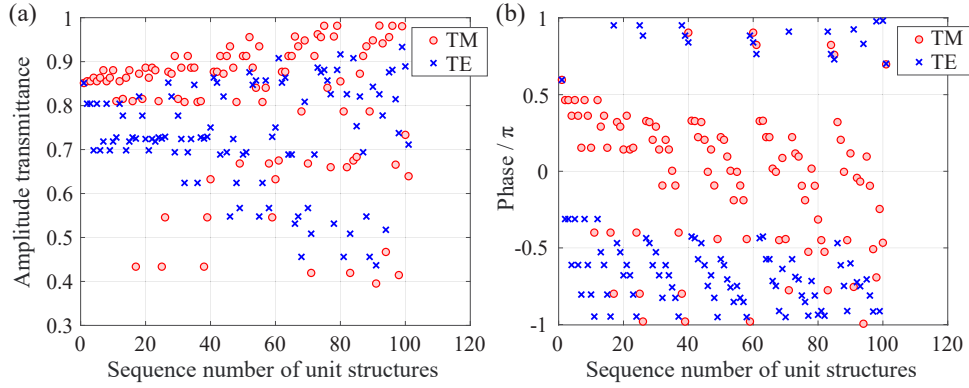


**Fig. 2.** (a) Amplitude transmittance of processable 2D units; (b) Modulated phases of processable 2D units.

where  $x$  is the radial coordinate of the metals,  $F$  is the focal length of the metals,  $\Psi$  is the phase constant with arbitrary value. In any interval  $(m-1)L \sim mL$  within the lens aperture, the unit with the largest projected value along the ideal complex amplitude in the structure library is selected as the optimal unit, as shown in Eq. (2). Compared with the principle of minimum complex amplitude deviation shown in Eq. (3), the principle of maximum projection can improve the focusing efficiency to a greater extent under the condition of limited TE state phase modulation.

$$\text{Max } \gamma_m = \text{real}[\tilde{E} \cdot \tilde{E}_0^*(mL + L/2)] \quad (2)$$

$$\text{Min } \gamma_m = |\tilde{E} - \tilde{E}_0(mL + L/2)|^2 \quad (3)$$

Both  $W_{\text{TE}}$  and  $W_{\text{TM}}$  are non-zero means that dual polarization state focusing is taken into account. At this time, the phase constant difference between TM and TE states, defined as  $\Delta\Psi = \Psi_{\text{TE}} - \Psi_{\text{TM}}$ , will affect the overall focusing effect of the metals. The point-by-point merit function is defined as the weighted sum of the complex amplitude projection of the two polarization states, as shown in Eq. (4).

$$\text{Max } \gamma_m = W_{\text{TM}} \cdot \text{real}[\tilde{E}_{\text{TM}} \cdot \tilde{E}_0^*(mL + L/2)] + W_{\text{TE}} \cdot \text{real}[\tilde{E}_{\text{TE}} \cdot \tilde{E}_0^*(mL + L/2) \cdot \exp(-i\Delta\Psi)] \quad (4)$$

Based on the above unit selection principle, the overall complex amplitude projection is obtained, as shown in Eq. (5), where  $D$  is the diameter of the metals.

$$\Gamma(\Delta\Psi) = \sum_{m=1}^{D/2L} \gamma_m \quad (5)$$

By adjusting  $\Delta\Psi$  in the range of  $(-\pi, \pi]$ , the sum of complex amplitude projection  $\Gamma(\Delta\Psi)$  can be taken as a maximum, and the corresponding 2D structure is the optimal result under the current weight allocation. By rotating the 2D structure around the optical axis, the overall 3D structure of the concentric-ring metals can be obtained, and the schematic diagram is shown in Fig. 3(a).

According to the scheme, a series of concentric-ring metalenses with  $D = 2$  cm,  $\text{NA} = 0.45$ , but different polarization weight allocations were assembled. The normal incidence focusing efficiency (the encircled power within  $3 \times \text{FWHM}$  of the focal spot divided by the near-field outgoing power) is used as the evaluation index of focusing performance, which is recorded emphatically as TE, TM and mixed wave of equal intensity are incident, as shown in Fig. 3(b). Therein, the focusing efficiencies as  $W_{\text{TE}} = 0, 1, 0.5$  are shown in Table 1. It can be seen that the focusing efficiency of the two polarization states is positively correlated with the corresponding

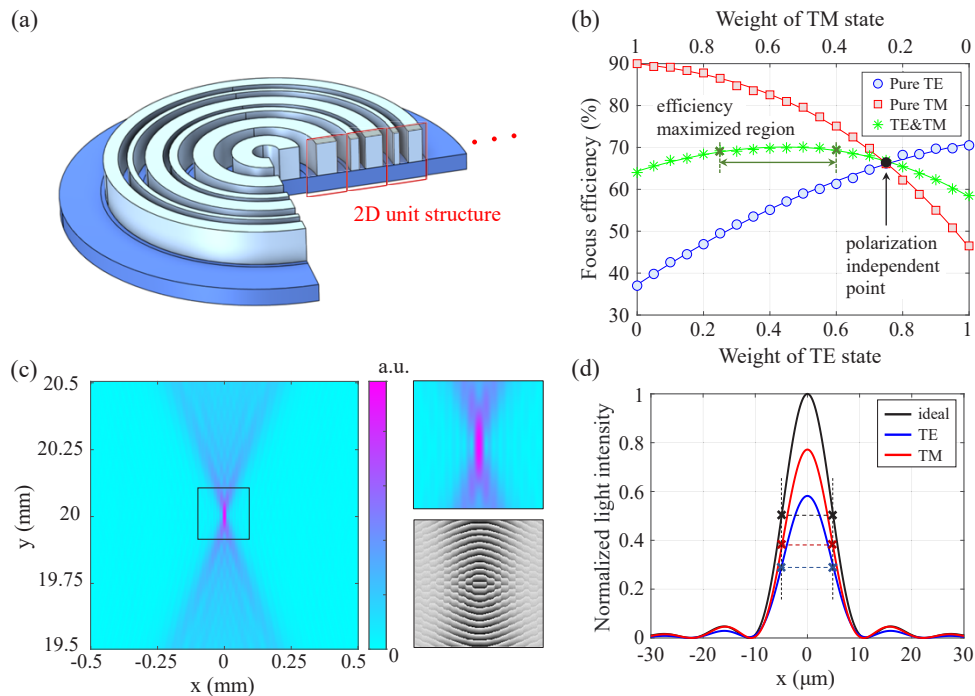


**Fig. 3.** (a) Schematic diagram of the 3D structure profile of the concentric-ring metalens; (b) The focusing efficiencies of the metalenses with different weight settings at pure TE, TM and mixed wave of equal intensity incident; (c)  $|E|$ -field near the focal point. The right subgraph shows the enlarged view and corresponding phase in the black box on the left; (d) Point Spread Function for different polarizations and ideal focusing.

weights, and the upper limit of the focusing efficiency of the single TM state can reach 90%, which, as far as we know, is very high in the technical framework of the binary-height concentric-ring metalens. The upper limit of focusing efficiency of TE wave is lower than that of TM, which is caused by the fact that 2D waveguide cannot support  $2\pi$  phase modulation of TE wave under the current structural height. Simply increasing the structural height to solve this problem poses significant machining challenges. Meanwhile, if the structural height and feature size are proportionally increased (the aspect ratio is constant), the increase in focusing efficiency due to higher concentric ring will be offset by the negative effect from larger feature sizes. Taking into account the above factors comprehensively, the selection of parameters such as the structural height, feature size, and aspect ratio of the concentric ring in this work are determined after balancing the processing difficulty and modulation performance, making the concentric-ring metalens have the optimal practicability.

**Table 1. Focusing efficiencies under typical incident light conditions with different weight allocations.**

Incident wave	Pure TE	TE and TM with equal intensity	Pure TM
$W_{TE} = 1$	71%	59%	46%
$W_{TM} = 1$	37%	64%	90%
$W_{TE} = W_{TM} = 0.5$	59%	70%	79%

TE and TM waves represent radially and tangentially polarized vector waves respectively in the 3D cylindrical symmetry model, and their equal intensity incidence represents the incidence of unpolarized light. In order to maximize the focusing efficiency of unpolarized light, the metalens with  $W_{TE} = W_{TM} = 0.5$  in the efficiency maximized region (Fig. 3(b)) is analyzed in depth. The  $|E|$ -field and PSF are shown in Fig. 3(c) and 3(d) respectively. The focal spot size of the two polarization states is close to the diffraction limit size, and the lost energy is uniformly dispersed on the focal plane, which will not appear as diffraction sidelobes and cause severe imaging blurring. In addition, the metalens only shows weak polarization dependence on vector polarized light, and show polarization independence for any scalar polarized light. Therefore, it is undoubtedly more meaningful to conduct subsequent processing and testing focusing on the above metalens with maximized focusing efficiency rather than that at the completely polarization independent point in Fig. 3(b).

In order to accurately evaluate the performance of the above 2D unit splicing method, a reverse design model for the global structure is established based on the topology optimization (TO) algorithm which is widely used in metasurface design [24,25]. With the TO model, another concentric-ring metalens with the same design wavelength, material, diameter, NA, structural height and feature size was designed as a performance reference. The weights of TE and TM waves were set to be equal, while the figure of merit (FoM) was determined by Strehl ratio (SR). The material density in the design domain was evolved through the adjoint sensitivity analysis [26,27], while the Helmholtz filtering method was used to constrain the feature size and the stepwise doubled projection slope  $\beta$  was used to gradually increase the interface clarity. Eventually, the material density converged, achieving binarization while maximizing the FoM, and ensuring that the feature size adhered to the processing requirements. The evolution process of the material density is shown in Fig. 4.

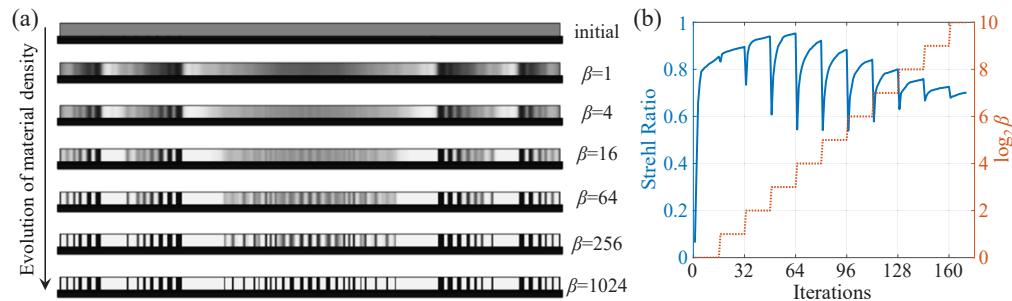


**Fig. 4.** (a) Schematic diagram of the material density evolution of a small concentric-ring metalens with a diameter of 0.2 mm (1% of the actual diameter); (b) The trend plot of SR, whose value oscillates as the boundary clarity constraint is enhanced stepwise.

The focusing efficiency of the TO concentric-ring metalens for unpolarized light is 71% in the simulation test, which indicates that the concentric-ring metalens obtained by the 2D unit splicing has almost the same focusing performance as the global optimization results. In terms of computing resource consumption, the 2D unit splicing metalens only required tens of seconds, whereas the global structure calculation process for the TO metalens took over more than two weeks on a computer node with 64 cores, 256GB memory and 3.0 GHz dominant frequency. The 2D unit splicing method has such a huge advantage in saving computing resources that concentric-ring metalenses with  $10^3\lambda$  or even  $10^5\lambda$  diameters can be easily designed. In addition, building the overall 2D cross-section using units with multi-wavelength in width is an appropriate compromise between the above two design methods [28], in which larger units ( $2\lambda\sim 4\lambda$  in width) with linear phase profiles are used instead of subwavelength units with constant phase. This scheme also maintains a high focusing efficiency (93% for metalens with  $D = 200\mu\text{m}$ ,  $\lambda=640\text{nm}$ ),

however, the consumption of computing resources is not compressed to the extreme (10 hours for metalens with  $D = 10^3 \lambda$ ) as TO is still required for unit structure design.

### 3. Fabrication process

The fabrication process of the concentric-ring metalens is shown in Fig. 5. According to the designed configuration ( $D = 2$  cm,  $H = 4.13 \mu\text{m}$  and feature size is  $0.69 \mu\text{m}$ ), the generally applicable I-line step lithography process was adopted since it can meet the needs of large-area manufacturing. The equipment used was Nikon I10 system with 22 mm main field, which can complete the graphics of the diameter 20 mm metalens in a single lithography process. The photoresist adopted S1805 positive resist with a resolution of 500 nm and the thickness up to 3500 nm. And the etching selection ratio with silicon is greater than 1:10, hence the etching depth of nanoring can be fully satisfied. The STS-HRM (B102) system with etching uniformity less than 5%, side wall perpendicularity better than  $87^\circ$  was chose for the deep silicon etching (DRIE).

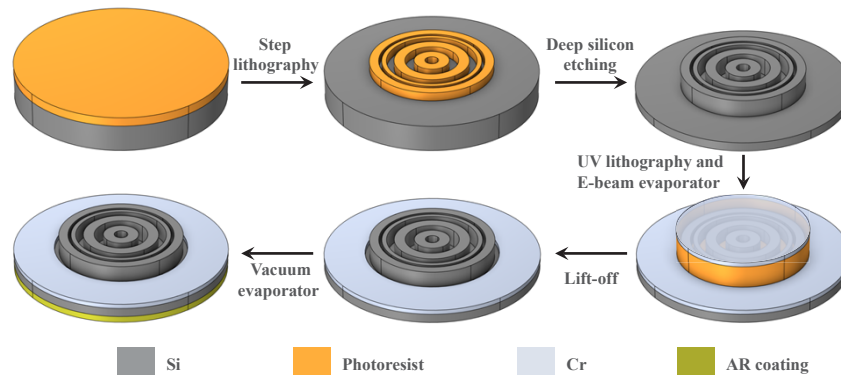


**Fig. 5.** Schematic diagram of the machining process of a concentric-ring metalens.

After the concentric-ring structures of the metalenses were processed, integrated Cr diaphragms with thickness of 300 nm were made on the same side of the metalenses, which adopted UV lithography process combined with electron beam evaporator (EB) to achieve the lift-off process. Considering the alignment accuracy of the UV lithography process is  $\pm 0.5 \mu\text{m}$ , the aperture of the diaphragm was set to 20.01 mm to prevent the diaphragm from damaging the structure inside. Finally, single-sided AR coatings were grown on the back of the metalenses by vacuum evaporator process, so that the broadband average transmittance of the silicon wafers at 8-12  $\mu\text{m}$  wavelength was increased from 55% to 65%. The morphological characterization results of the fabricated concentric-ring metalens are shown in the Fig. 6. The width and height of the simulated concentric rings are both integer multiples of  $L_m$ , thus it can be seen that the size error is generally controlled within 70 nm (about  $0.2L_m$ ). The influence of the corresponding random phase error on the focusing efficiency is completely within the acceptable range (less than 3%), and the location and morphology of the focal spot are almost not affected.

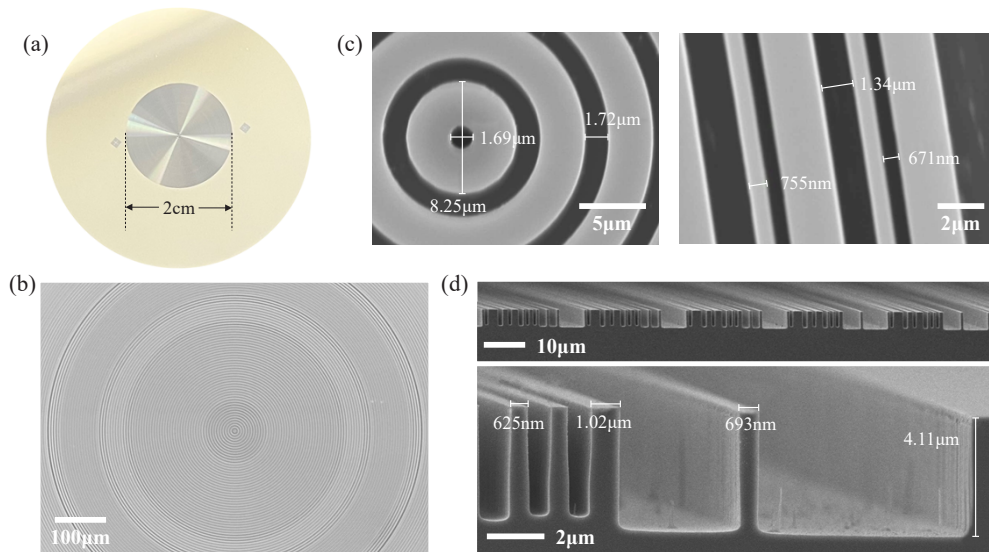


**Fig. 6.** (a) Physical image of the concentric-ring metalens; (b) Low magnification top view of the central area; (c) High magnification top view of central and edge areas; (d) Side view and partial enlargement of concentric-ring section in edge area.

#### 4. Thermal imaging test

A LWIR imaging test system was built by combining the fabricated metalens and a LWIR array detector (MicroIII 384 T, IRay Technology Co., Ltd.), and the blackbody radiation system (HT0526A, Taian Hart Instrumentation Co., Ltd.) is used as the observation target. In addition, a LWIR commercial camera (IRS-FB435-T, IRay Technology Co., Ltd.) based on traditional optical lens groups is used for performance comparison, whose focal length is 19 mm,  $F\#$  is 1, which is very close to the parameters of the metalens in this work. The LWIR cameras and the blackbody radiation system are shown in Fig. 7.

In order to test the resolution of the LWIR camera based on the concentric-ring metalens, the temperature of the target and the blackbody radiation source behind it are set to 25°C and 80°C, respectively, so as to ensure that the observed light and dark fringes have a fixed radiation intensity ratio. By adjusting the spatial frequency of the target and its distance to the camera, imaging targets with different angular spatial frequencies are formed. The imaging renderings of commercial camera and metalens camera for the targets with different angular spatial frequencies are shown in the first two rows of the subgraphs in Fig. 8. The image produced by the metalens camera exhibits lower clarity due to the influence of chromatic aberration. Considering the wide spectrum characteristics of blackbody radiation, single narrowband filtering will not cause identifiable adverse effects on target recognition and temperature testing [29,30]. To this end, a filter with a central wavelength of 10µm and a bandwidth of 1.5µm is installed in front of the metalens, and the imaging renderings is shown in the third row of Fig. 8. Furthermore, the stray light generated by non-first-order diffraction is almost evenly distributed on the image plane, resulting in a noticeable basic gray response on the image plane, which affects the intensity contrast of the images. After removing the stray background and establishing steeper gray linear mapping at the software level, the new imaging effect is shown in the fourth row of Fig. 8. The test scatter points and their polynomial fitting curves of the relationship between intensity contrast and angular resolution under four different camera settings are shown in the Fig. 9(a). The

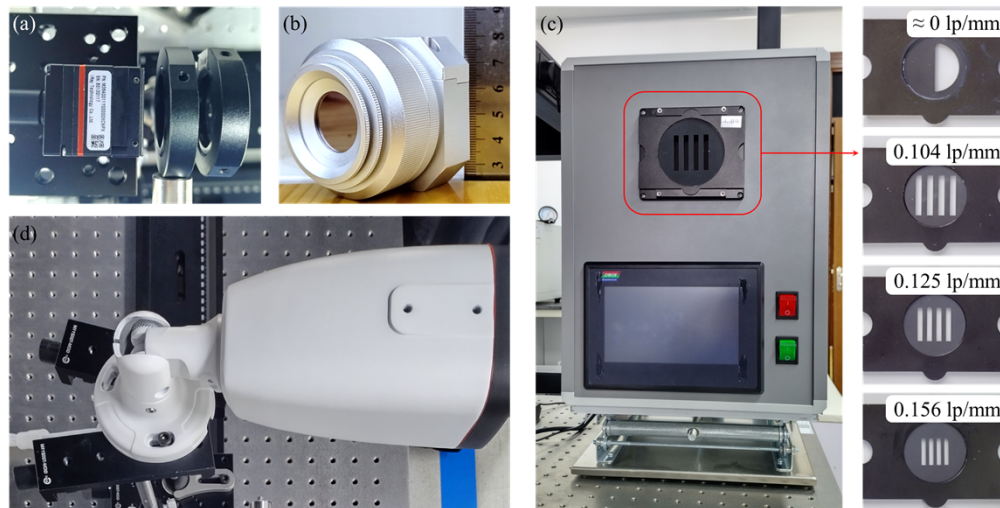


**Fig. 7.** (a) The infrared imaging system composed of narrowband filters, concentric-ring metalens and LWIR array detectors; (b) The LWIR imaging prototype packaged after the total length of the optical system in (a) is further compressed; (c) Blackbody radiation system and some alternative contrast test targets with different spatial resolutions; (d) The LWIR commercial cameras for imaging performance comparison.

personal imaging effects with narrow-band filtering and gray remapping are shown in Fig. 9(b) and Fig. 9(c).

Angular spatial frequency (lp/mrad)	0	0.0446	0.0625	0.0982	0.1375
Commercial camera					
Metalens camera					
Metalens camera with narrowband filter					
Introducing linear re-mapping of graylevels					

**Fig. 8.** Imaging results of typical resolution targets by different imaging methods.

It can be seen that narrowband filters can effectively improve the intensity contrast in low-frequency regions. Further compression of the filter bandwidth can theoretically expand the

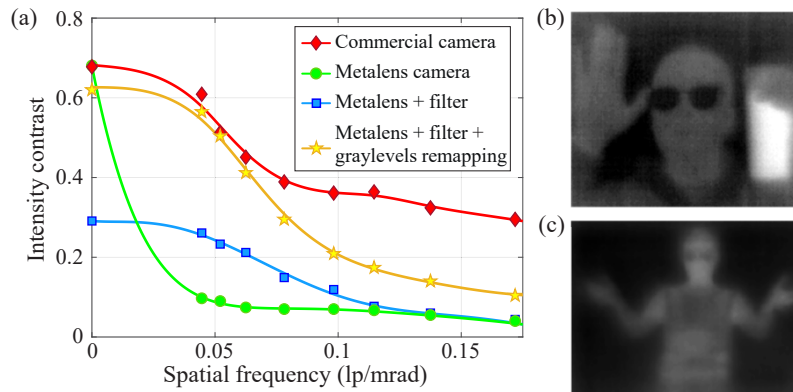


**Fig. 9.** (a) Intensity contrast scatter and polynomial fitting curves for different camera Settings. (b) Imaging effect of an experimenter holding an 80°C water cup at a distance of 1 m from the camera; (c) Imaging effect of the experimenter at a distance of 3 m from the camera.

range of contrast enhancement to the high-frequency end, but the actual imaging effect is limited by the signal-to-noise ratio and has not achieved a recognizable improvement. After further introducing linear remapping of image grayscale, the intensity contrast is approximately doubled within the frequency range, and the imaging effect is improved to a level comparable to that of commercial cameras in the low-frequency region, which enables the camera to effectively distinguish the outline and clothing details of the person being tested several meters away, while ensuring temperature measurement accuracy.

After determining the image gray remapping relationship, temperature calibration was carried out within the imaging distance of 0.5 m to 1.1 m to realize the temperature measurement function. The blackbody test scatter of gray-temperature relationship and the polynomial fitting curve after gray remapping are shown in Fig. 10(a). The gray-temperature curve exhibits an approximately linear change within the imaging distance range, so the temperature of the blackbody at any distance within the range can be measured by the linear interpolation method.

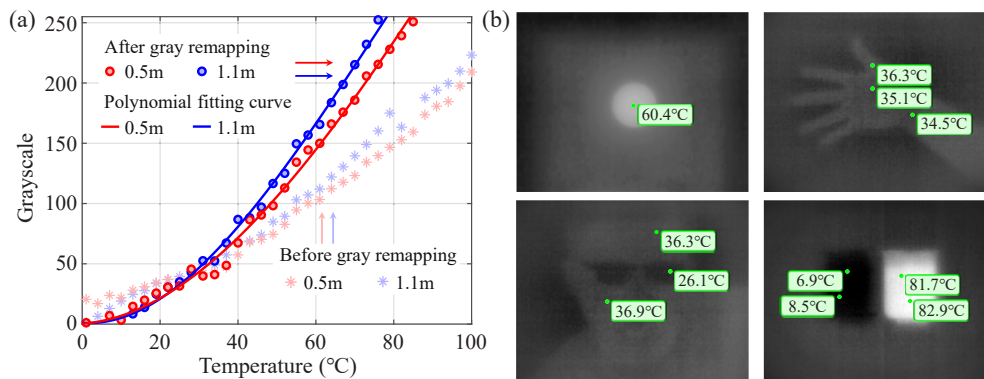


**Fig. 10.** (a) Gray-temperature relationship before and after gray remapping (b) Temperature test results of black body (60°C), human body (36.5°C), glass (8°C and 81 °C).

Despite the slight compression of the temperature measurement range (from  $-10^{\circ}\text{C}$ ~ $120^{\circ}\text{C}$  to  $0^{\circ}\text{C}$ ~ $85^{\circ}\text{C}$ ) through gray remapping in the metalens camera, there is a notable improvement in image contrast and temperature measurement accuracy, with a measurement error of  $\leq 2^{\circ}\text{C}$ .

Follow-up work will continue to enrich the calibration information such as detection distance and emissivity for different targets, and the measurement accuracy will be further improved to the level of existing commercial temperature measuring instruments.

## 5. Conclusion

In this article, a 2D subwavelength unit splicing method is proposed to design the cross-sectional structure of concentric-ring metalenses. Compared with the global optimization method, the proposed design method exhibits a significant decrease in time cost and computational power consumption by several orders of magnitude, while the focusing efficiency has hardly deteriorated. This characteristic bestows great advantages upon the design of concentric-ring metalenses with diameters ranging from  $10^3$  to  $10^5$  wavelengths. After encapsulating the processed metalens, narrowband filter and commercial LWIR detector, the volume and weight of the resulting LWIR camera are reduced to less than 10% of those found in commercial cameras equipped with traditional optical lens groups. Moreover, the imaging contrast in the low-frequency region closely approximates that of commercial cameras, and the temperature measurement accuracy is achieved at less than 2°C. The proposed method greatly reduces the development cost of concentric-ring metalenses, further enhances their market competitiveness and expands their application prospects in compact imaging instruments.

**Funding.** National Natural Science Foundation of China (51875545); Jilin Scientific and Technological Development Program (SKL202302020); CAS Project for Young Scientists in Basic Research (YSBR-066).

**Acknowledgments.** This work was supported by Changchun Institute of Optics, Fine Mechanics and Physics, Chinese Academy of Sciences(CIOMP) and the National Natural Science Foundation of China.

**Disclosures.** The authors declare no conflicts of interest.

**Data availability.** Data underlying the results presented in this paper are not publicly available at this time but may be obtained from the authors upon reasonable request.

## References

1. M.L. Tseng, H.H. Hsiao, C.H. Chu, M.K. Chen, G. Sun, A.Q. Liu, and D.P. Tsai, "Metalenses: Advances and Applications," *Adv. Opt. Mater.* **6**(18), 1800554 (2018).
2. P. Genevet, F. Capasso, F. Aieta, M. Khorasaninejad, and R. Devlin, "Recent advances in planar optics: from plasmonic to dielectric metasurfaces," *Optica* **4**(1), 139–152 (2017).
3. M. Khorasaninejad, W.T. Chen, R.C. Devlin, J. Oh, A.Y. Zhu, and F. Capasso, "Metalenses at visible wavelengths: diffraction-limited focusing and subwavelength resolution imaging," *Science* **352**(6290), 1190–1194 (2016).
4. C.M. Soukoulis and M. Wegener, "Past achievements and future challenges in the development of three-dimensional photonic metamaterials," *Nat. Photonics* **5**(9), 523–530 (2011).
5. M. Pan, Y. Fu, M. Zheng, H. Chen, Y. Zang, H. Duan, Q. Li, M. Qiu, and Y. Hu, "Dielectric metalens for miniaturized imaging systems: progress and challenges," *Light: Sci. Appl.* **11**(1), 195 (2022).
6. N. Yu and F. Capasso, "Flat optics with designer metasurfaces," *Nat. Mater.* **13**(2), 139–150 (2014).
7. N. Yu, P. Genevet, M.A. Kats, F. Aieta, J.P. Tetienne, F. Capasso, and Z. Gaburro, "Light Propagation with Phase Discontinuities: Generalized Laws of Reflection and Refraction," *Science* **334**(6054), 333–337 (2011).
8. F. Aieta, M.A. Kats, P. Genevet, and F. Capasso, "Multiwavelength achromatic metasurfaces by dispersive phase compensation," *Science* **347**(6228), 1342–1345 (2015).
9. S. Wang, P.C. Wu, V.C. Su, Y.C. Lai, M.K. Chen, H.Y. Kuo, B.H. Chen, Y.H. Chen, T.T. Huang, J.H. Wang, R.M. Lin, C.H. Kuan, T. Li, Z. Wang, S. Zhu, and D.P. Tsai, "A broadband achromatic metalens in the visible," *Nat. Nanotechnol.* **13**(3), 227–232 (2018).
10. Y. Wang, Q. Chen, W. Yang, Z. Ji, L. Jin, X. Ma, Q. Song, A. Boltasseva, J. Han, V.M. Shalaev, and S. Xiao, "High-efficiency broadband achromatic metalens for near-IR biological imaging window," *Nat. Commun.* **12**(1), 5560 (2021).
11. W.T. Chen, A.Y. Zhou, V. Sanjeev, M. Khorasaninejad, Z. Shi, E. Lee, and F. Capasso, "A broadband achromatic metalens for focusing and imaging in the visible," *Nat. Nanotechnol.* **13**(3), 220–226 (2018).
12. S. Wang, P.C. Wu, V.C. Su, Y.C. Lai, C.H. Chu, J.W. Chen, S.H. Lu, J. Chen, B. Xu, C.H. Kuan, T. Li, S. Zhu, and D.P. Tsai, "Broadband achromatic optical metasurface devices," *Nat. Commun.* **8**(1), 187 (2017).
13. R. Paniagua-Domínguez, Y.F. Yu, E. Khaidarov, S. Choi, V. Leong, R.M. Bakker, X. Liang, Y.H. Fu, V. Valuckas, L.A. Krivitsky, and A.I. Kuznetsov, "A Metalens with a Near-Unity Numerical Aperture," *Nano Lett.* **18**(3), 2124–2132 (2018).

14. Y.Q. Liu, Z. Ren, Y. Shu, L. Wu, J. Sun, H. Cai, X. Zhang, L. Lu, K. Qi, L. Li, Y. Che, and H. Yin, "Broadband, large-numerical-aperture and high-efficiency microwave metalens by using a double-layer transmissive metasurface," *Appl. Phys. Express* **15**(1), 014003 (2022).
15. Y. Xie, J. Zhang, S. Wang, and D. Liu, "High-efficiency broadband photonic crystal fiber metalens with a large numerical aperture," *Opt. Commun.* **481**, 126524 (2021).
16. X. Ou, T. Zeng, Y. Zhang, Y. Jiang, Z. Gong, F. Fan, H. Jia, H. Duan, and Y. Hu, "Tunable Polarization-Multiplexed Achromatic Dielectric Metalens," *Nano Lett.* **22**(24), 10049–10056 (2022).
17. Y. Hu, X. Ou, T. Zeng, J. Lai, J. Zhang, X. Li, X. Luo, L. Li, F. Fan, and H. Duan, "Electrically Tunable Multifunctional Polarization-Dependent Metasurfaces Integrated with Liquid Crystals in the Visible Region," *Nano Lett.* **21**(11), 4554–4562 (2021).
18. H. He, H. Yang, Z. Xie, and X. Yuan, "Broadband mid-infrared metalens with polarization-controlled at-will chromatic dispersion," *Nanoscale* **14**(34), 12476–12482 (2022).
19. C. Hao, S. Gao, Q. Ruan, Y. Feng, Y. Li, Joel K. W. Yang, Z. Li, and C. W. Qiu, "Single-Layer Aberration-Compensated Flat Lens for Robust Wide-Angle Imaging," *Laser Photon. Rev.* **14**(6), 2000017 (2020).
20. G. Cao, X. Gan, Han, Lin, and B. Jia, "An accurate design of graphene oxide ultrathin flat lens based on Rayleigh-Sommerfeld theory," *Opto-Electron. Adv.* **1**(7), 18001201 (2018).
21. R. E. Christiansen, Z. Lin, C. Roques-carmes, Y. Salamin, S.E. Kooi, J.D. Joannopoulos, M. Soljačić, and S.G. Johnson, "Fullwave Maxwell inverse design of axisymmetric, tunable, and multi-scale multi-wavelength metalenses," *Opt. Express* **28**(23), 33854–33868 (2020).
22. Z. Lin, C. Roques-Carmes, R.E. Christiansen, M. Soljačić, and S.G. Johnson, "Computational inverse design for ultra-compact single-piece metalenses free of chromatic and angular aberration," *Appl. Phys. Lett.* **118**(4), 041104 (2021).
23. X. Xiao, Y. Zhao, X. Ye, C. Chen, X. Lu, Y. Rong, J. Deng, G. Li, S. Zhu, and T. Li, "Large-scale achromatic flat lens by light frequency-domain coherence optimization," *Light: Sci. Appl.* **11**(1), 323 (2022).
24. L. Zhang, C. Wang, Y. Wei, Y. Lin, Y. Han, and Y. Deng, "High-Efficiency Achromatic Metalens Topologically Optimized in the Visible," *Nanomaterials* **13**(5), 890 (2023).
25. D. Sell, J. Yang, S. Doshay, R. Yang, and J.A. Fan, "Large-Angle, Multifunctional Metagratings Based on Freeform Multimode Geometries," *Nano Lett.* **17**(6), 3752–3757 (2017).
26. Y. Deng and J.G. Korvink, "Self-consistent adjoint analysis for topology optimization of electromagnetic waves," *J. Comput. Phys.* **361**, 353–376 (2018).
27. Z. Jin, Y. Lin, C. Wang, Y. Han, B. Li, J. Zhang, X. Zhang, P. Jia, Y. Hu, Q. Liu, H. Duan, J.G. Korvink, Y. Li, H. Jiang, and Y. Deng, "Topologically optimized concentric-nanoring metalens with 1 mm diameter, 0.8 NA and 600 nm imaging resolution in the visible," *Opt. Express* **31**(6), 10489–10499 (2023).
28. T. Phan, D. Sell, E.W. Wang, S. Doshay, K. Edee, J. Yang, and J.A. Fan, "High-efficiency, large-area, topology-optimized metasurfaces," *Light: Sci. Appl.* **8**(1), 48 (2019).
29. M. Meem, S. Banerji, A. Majumder, F.G. Vasquez, B. Sensale-Rodriguez, and R. Menon, "Broadband lightweight flat lenses for long-wave infrared imaging," *Proc. Natl. Acad. Sci. U. S. A.* **116**(43), 21375–21378 (2019).
30. L. Huang, Z. Coppens, K. Hallman, Z. Han, K.F. Böhringer, N. Akozbek, A. Raman, and A. Majumdar, "Long wavelength infrared imaging under ambient thermal radiation via an all-silicon metalens," *Opt. Mater. Express* **11**(9), 2907–2914 (2021).